Hindawi
Advances in Materials Science and Engineering
Volume 2019, Article ID 3251590, 11 pages
https://doi.org/10.1155/2019/3251590

Research Article

Optimization of Structure Parameters of Airfield Jointed Concrete Pavements under Temperature Gradient and Aircraft Loads

Bangshu Xu,[1] Wanzhi Zhang,[1] Jie Mei,[1] Guangyao Yue,[1] and Laihua Yang[2]

[1]*Research Center of Geotechnical and Structural Engineering, Shandong University, Jinan 250061, China*
[2]*China Railway 12th Bureau Group Co., Ltd., Taiyuan 030024, China*

Correspondence should be addressed to Wanzhi Zhang; zwzwanzhi@163.com

Received 6 November 2018; Accepted 25 March 2019; Published 24 April 2019

Guest Editor: Roberto Brighenti

Daily changing temperature causes significant thermal stress in concrete pavement. Tensile stress obtained can exceed flexural tensile strength when the concrete slabs are subjected to large temperature gradient and traffic loads, resulting in pavement damages. In this paper, maximum tensile stresses in concrete slabs with different slab sizes, thicknesses, and length to width (L/W) ratios were investigated by using the finite element (FE) method. The important parameters in the design of concrete pavement are the flexural tensile strength and the fatigue limit. By analyzing the comparison results between the maximum tensile stress and the fatigue limit, the optimum slab size and the critical thickness were determined. The results indicate that the maximum tensile stress obtained is higher for larger slab size with thin thickness. Furthermore, to reduce cutting work and the amount of dowel bars, the optimum slab sizes of the regional airport concrete pavement are recommended as 4 m × 4 m to 6 m × 6 m. The critical thicknesses of 4 m × 4 m slab and 6 m × 6 m slab are determined as 28.2 cm and 34.7 cm, respectively, based on the most unfavorable coupling between positive and negative temperature gradients and the Boeing 737–800 aircraft load. Moreover, the maximum tensile stress increases as the L/W ratio increases. When the slab length is less than 6 m, it is better to use square slab in airport jointed concrete pavement (JCP).

1. Introduction

In the recent years, concrete pavements are preferred because of their high strength, good durability, less maintenance, and ease of procurement. In China, approximately 90% of civil airport pavements are constructed with Portland cement concrete (PCC) [1, 2]. Airport concrete pavement, as a sheet and large area structure exposed to natural environment, bears the long-term damage from the external environment, such as atmospheric temperature, humidity, and solar radiation [3–5] and aircraft repeated loads [6], resulting in cracks, voids, and other defects [7]. Especially in the environment of large temperature difference between day and night, it is important to have a better understanding of the response of concrete pavement within its design life. Therefore, in the design of airport concrete pavement, airport authorities are interested in selecting the preferred pavement design considering environmental factors and performance requirements.

PCC pavements expand and contract in the horizontal plane under temperature changes. Meanwhile, PCC pavements show upward curling or downward curling under the influence of temperature gradients [8–10]. However, these movements will be restrained or resisted by self-weight of concrete slabs and friction between slab and layer below it, inducing significant thermal stresses in concrete slabs [11–13]. For JCP, the thermal stress magnitude is directly related to the structural parameters and the constraints of the concrete slab. Tian et al. studied the effect of the base types and the conditions of constraint between the slab and the base on the thermal stress [14]. The findings imply that the thermal stress in the slab of lean concrete base is the largest. Moreover, when the contact state between the slab

and the base changes from continuous to smooth, the thermal stress decreases significantly. Nam et al. proposed that subsurface conditions and joint/crack width affect the behavior and response of JCP [15]. It is noted that the slab tends to have smaller voids with the decreased subgrade modulus, and the longitudinal stress in its bottom edge increases as the crack width becomes tighter. Moreover, when concrete slabs are subjected to the combined action of the large temperature gradient and traffic loads, critical stresses may be developed. Many researchers have reported different slab sizes considering various factors. Huang suggested the sizes of concrete slabs are in the range of 15–30 ft (4.6–9.1 m) for JCP depending on the type of aggregate and climate [16]. Wei et al. suggested that the critical slab size of rural road concrete pavement was 2 m × 2 m considering the combined effect of 15°C temperature difference and 100 kN axes load [17]. Chattaraj and Pandey investigated critical stresses of square slabs of different sizes under dual wheel load using the FE method [18]. They proposed that critical stresses are drastically reduced for smaller slab size. A number of studies related to thicknesses of concrete slabs and L/W ratios have also been conducted. Al-Nasra and Wang [19] and Nam et al. [15] have also revealed that the thicker slab has a greater fluctuation in the edge vertical movement. Vishwakarma and Ingle studied the effect of different sizes and L/W ratios of concrete slabs on their critical stresses under temperature load, traffic load, and combined effect of temperature and traffic loads [20]. They concluded that the tensile stress increases with the increase in the slab length and width. Tensile stresses for L/W ratio 1.25 or below are almost the same. However, when L/W ratio exceeds 1.25, there is considerable increase in the maximum edge stress.

The objectives of the present studies are to evaluate the critical stresses and deformations of concrete slabs considering different structural parameters and combined effects of various temperature and traffic loads. The optimum slab sizes, thicknesses, and L/W ratios of regional airport JCP related to environmental temperature and aircraft loads still need to be investigated. It is especially important for environment temperature occurring in Northeast China significantly influencing tensile stresses of concrete slabs. Therefore, field temperature and strain tests of a regional airport concrete pavement in Northeast China were performed. In order to analyse in detail distributions of maximum tensile stresses of different slab sizes, thicknesses, and L/W ratios under the most unfavorable load-bearing positions, we applied three-dimensional (3-D) analyses using the FE method. Here, based on the comparison results between the maximum tensile stress and the fatigue limit, the optimum slab size and the critical thickness are determined and the square slab is recommended. The obtained results can be helpful in design of new regional airport JCP and assessment of their load in countries with big temperature amplitudes.

2. Field Experiment

2.1. Temperature and Strain Tests. Based on a regional airport concrete pavement project in Northeast China, distribution laws of temperature and strain fields in concrete slabs were monitored by embedding semiconductor temperature sensors and vibration wire strain sensors. Figure 1 shows the cross section of the pavement structure and the layout of the temperature and strain sensors. The airport pavement is composed of concrete slabs, cement-treated base (CTB), crushed-stone base (CSB), and subgrade (Table 1). The temperature and strain sensors are placed inside the concrete slab. The guideline of CACC (China Airport Construction Group Corporation) recommends that the reinforced concrete cover depth should not be less than 50 mm in the design of airport reinforced concrete pavements [21]. Therefore, the embedded temperature and strain sensors are placed at a distance of 60 mm from the surface and bottom of the concrete slab. The temperature and strain sensors are installed in the centre of the slab. In Figure 1(a), four temperature sensors (T60/T140/T220/T300, the number represents its depth) are arranged in the vertical direction and the vertical spacing is 80 mm. In Figure 1(b), two strain sensors are arranged at the surface and bottom, respectively, of which one (S60-1/S300-1) is in the transverse direction and the other (S60-2/S300-2) is in the longitudinal direction and the vertical spacing is 240 mm.

The temperature and strain data were collected continuously and automatically by using "Wireless transmission module JMTX-2014" and "DSC software platform." Data acquisition time was from August 1, 2016, to November 3, 2016, and the data acquisition interval was set to 1 h.

2.2. Distribution Laws of Temperature and Strain Fields. From August to November, the natural climate conditions in Northeast China change from midsummer to early winter and the ambient temperature significantly decreases. It is important to understand the behavior of concrete slabs under the environmental load including temperature gradient and environmental strain. Therefore, the temperature and strain data of a typical day with maximum temperature difference between day and night in August and November were adopted. The data are used to analyze the daily temperature variations, temperature gradient distributions along the depth, and the incremental relationships between strain and temperature.

2.2.1. Temperature Field Distributions. Figure 2 presents daily temperature variations over different months. The temperature fluctuation curves in the concrete slab are similar to sine function curves. The surface temperature exhibits extreme fluctuations. An increase in the depth successively decreases the amplitude of the temperature fluctuation. Figure 3 shows temperature gradient distributions along the depth over different months. Temperature distributions along the slab depth are nonlinear. The temperature gradients considerably vary at different times within a day. As shown in Figures 2 and 3, the maximum positive temperature difference between surface and bottom is approximately observed at 3 p.m. while the maximum negative temperature difference occurs at

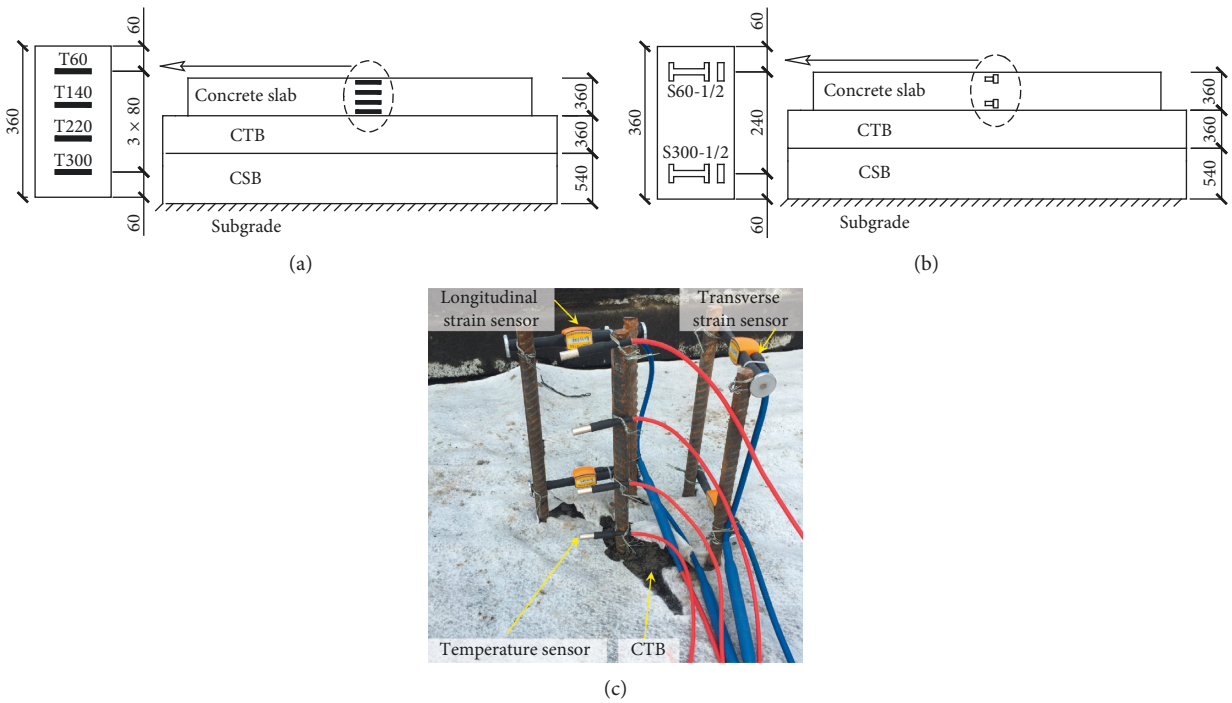

Figure 1: Pavement structure and layout of (a) temperature sensors (unit: mm) and (b) strain sensors (unit: mm). (c) Field layout of temperature and strain sensors.

Table 1: Structure parameters of airport pavement layers.

Pavement layers	Slab size (m)	Thickness (m)
Concrete slab	5 × 4.5	0.36
CTB	19 × 14	0.36
CSB	19 × 14	0.54
Subgrade	19 × 14	7.00

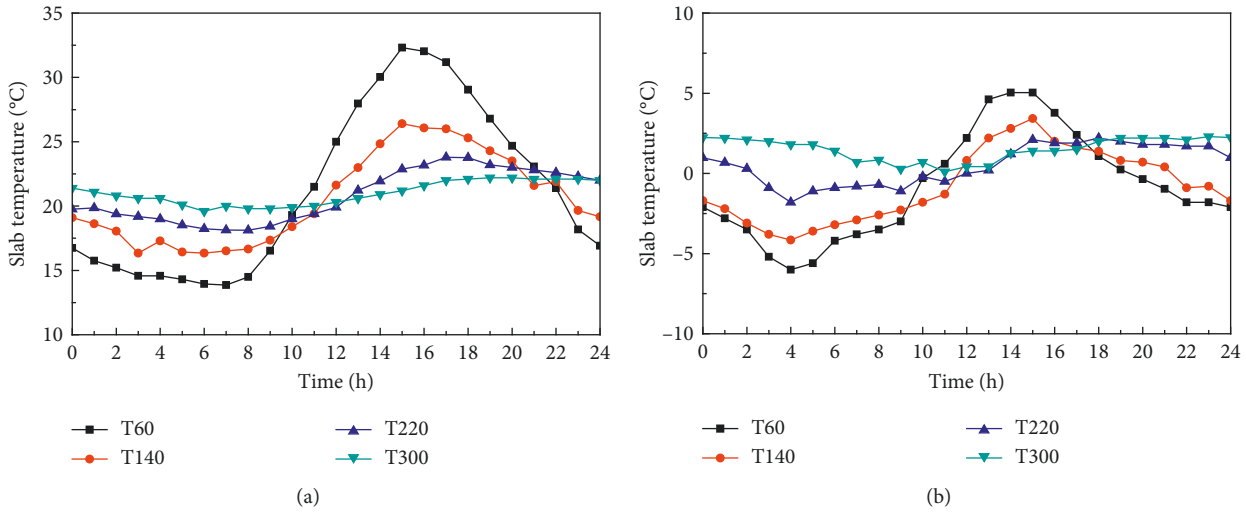

Figure 2: Temperature daily fluctuation curves in the concrete slab over different months. (a) August 14th. (b) November 2nd.

approximately 4 a.m. The maximum positive and negative temperature differences and corresponding temperature gradients are listed in Table 2.

2.2.2. Strain Field Distributions. Figure 4 shows the temperature-strain increment relationships in a typical day over different months. The hysteresis of temperature data

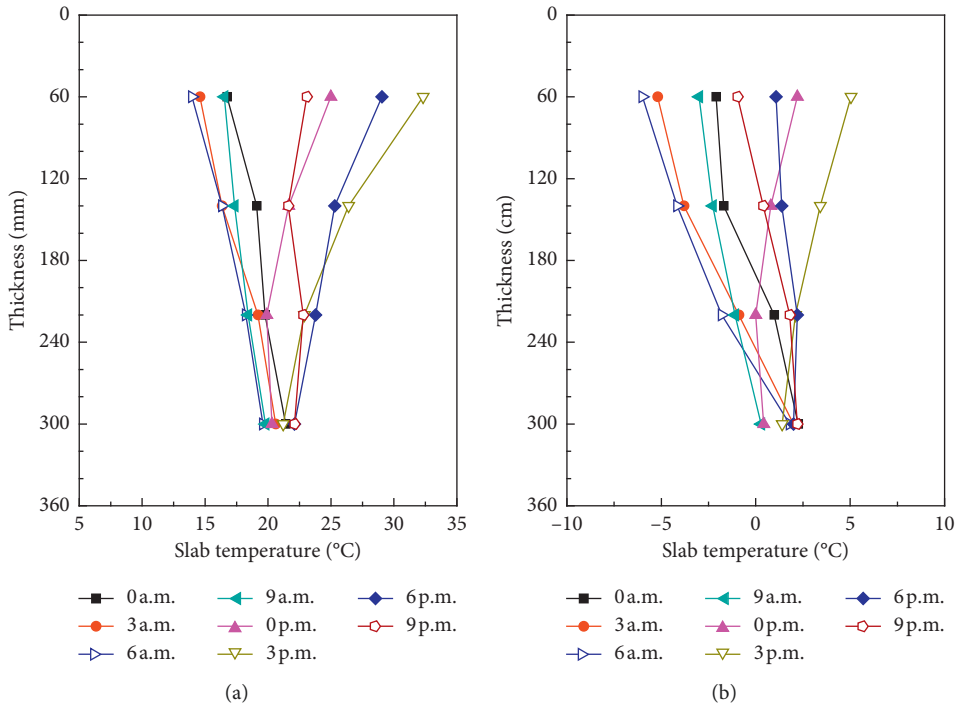

Figure 3: Nonlinear temperature gradient distribution in the concrete slab over different months. (a) August 14th. (b) November 2nd.

Table 2: Maximum temperature differences and temperature gradients in the concrete slab over different months.

Date	Positive		Negative	
	Temperature difference (°C)	Temperature gradient (°C·cm^{-1})	Temperature difference (°C)	Temperature gradient (°C·cm^{-1})
August 14th	12.1	0.50	−7.8	−0.33
November 2nd	4.6	0.19	−9.8	−0.41

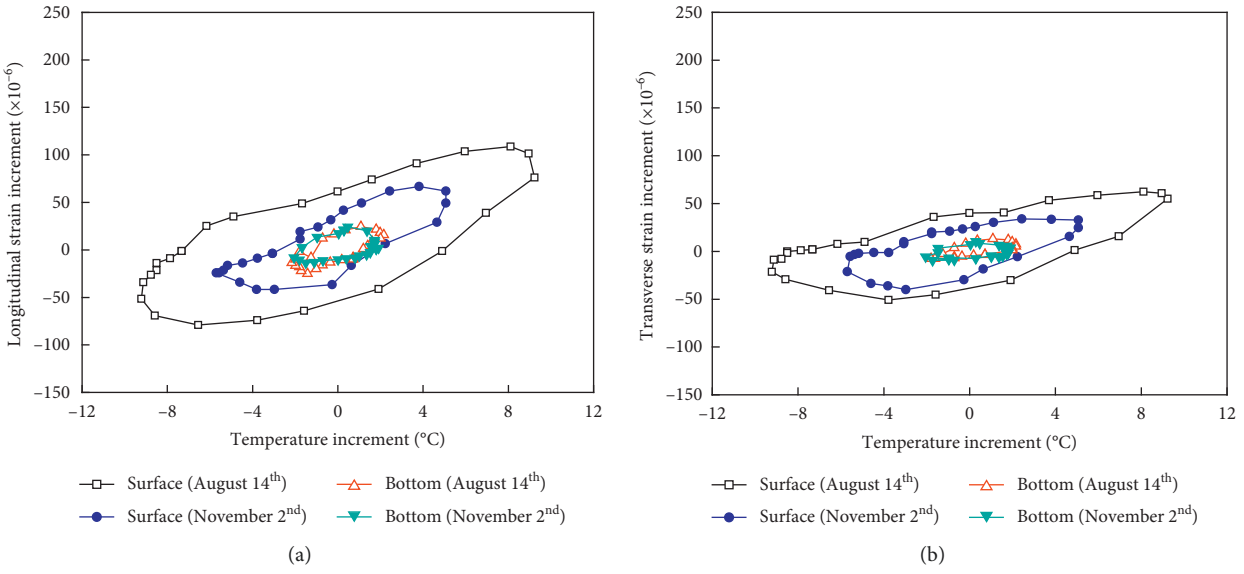

Figure 4: Relationships between the measured temperature-strain increments. (a) Longitudinal temperature-strain increments. (b) Transverse temperature-strain increments.

versus strain data is evident, and the paths of temperature increase and decrease do not coincide. When the increment of temperature is identical, a slight difference is observed between the longitudinal and transverse strain increments and the increment of transverse is smaller. The temperature-strain increment hysteresis loops of the bottom are significantly smaller than that of the surface due to the effect of slab thickness. The size of the temperature-strain increment hysteresis loops varies in different months under the influence of environment temperature.

3. Modeling and Validation of FE Model

3.1. Model and Mesh. To analyze the mechanical behaviors of concrete pavement given the measured temperature gradients, the 3-D FE model with nine concrete slabs was developed by using the FE software ABAQUS (Figure 5). In the numerical simulation, multilayer structures of pavement, self-weight, two different joint types (dowel joint and key joint), and the interlayer contact surfaces were modelled. The dowel joint has dowel bars, and the key joint has tension bars at the mid-depth of concrete slabs. The 27-node solid elements (C3D27R) was used to discretize the pavement layers and dowel bars and tension bars, which were widely used in related researches and recommended by the ABAQUS program for plane stress analysis [22–24]. Each node of the C3D27R element has three degrees of freedom (U_x, U_y, and U_z). The C3D27R was used such that the accuracy of the mechanical calculation is not evidently affected when the element meshes are distorted in numerical analysis.

3.2. Pavement Layers and Material Parameters. The sizes of pavement layers are listed in Table 1. According to geological exploration data and geotechnical tests, the material parameters of pavement layers are summarized in Table 3. The coefficient of thermal expansion (CTE) used in the FE analysis was estimated by backcalculation by using the measured temperature-strain increment data (Figure 4). The first-order polynomial of the least squares method is used to obtain the average of CTE of the concrete mixture. In this study, the CTE is 9.86×10^{-6}/°C.

3.3. Temperature Field in the FE Models. From the temperature measurement results (Figure 3), the nonlinear distribution of temperature is not negligible in the numerical analysis. Choubane and Tia proposed that the temperature nonlinear distribution throughout the whole depth of concrete slab can be adequately described by quadratic function as follows [25]:

$$T(z) = A + Bz + Cz^2, \tag{1}$$

where A, B, and C are coefficients and z is the distance from the slab surface.

The temperature gradients of $50^{\circ}\text{C}\cdot\text{m}^{-1}$ and $-41^{\circ}\text{C}\cdot\text{m}^{-1}$ were applied. Equation (1) was used to fit the nonlinear distribution of positive and negative temperature gradients in concrete slabs based on the temperature data measured at 6 a.m. and 3 p.m. (Figure 3). In the FE models, it is assumed that the temperature of the whole base is a fixed value, which is the bottom temperature of the concrete slab at the corresponding time.

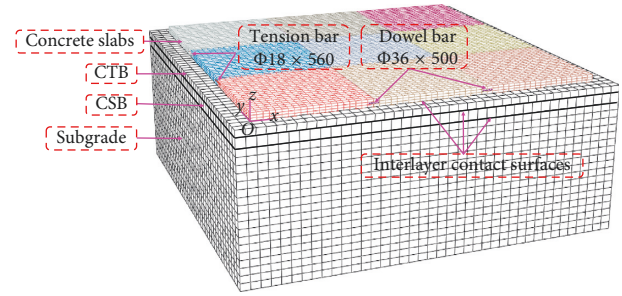

Figure 5: 3-D FE model for test slabs (unit: mm).

3.4. Interlayer Contact Relations and Boundary Conditions. The isotropic Coulomb friction model is used to simulate the tangential bond slip between the pavement layers. The airport pavement test section is a new concrete pavement, and thus, the contact between each layer is good. In the FE models, the friction coefficient is set to 1, and this implies that the layers are continuous. The normal contact between layers is set to the hard contact. Meanwhile, according to the researches of Tian et al. and Nam et al. [14, 15], the smaller the joint width of adjacent slabs, the larger the stress in the concrete pavement under the same temperature load. Therefore, the two adjacent slabs are simulated as full contact.

The symmetrical boundary condition is set in x-axis, and the free boundary condition is set in y-axis for the concrete slabs. The bottom of the subgrade layer is modelled as fixed with respect to the x, y, and z directions. The sides of the CTB, CSB, and subgrade are x- and y-axes symmetrical boundary conditions. Dowel bars were arranged in the transverse joints (dowel joints), and tension bars were placed in the longitudinal joints (key joints).

3.5. Model Validation. Based on the temperature and strain data and the elastic thin plate theory, the measured stresses of the test slab are calculated as follows [26]:

$$\sigma_x = -\frac{E}{1-\nu^2}\left(\varepsilon_x + \nu\varepsilon_y\right) - \frac{E\alpha T(z)}{1-\nu}, \tag{2}$$

$$\sigma_y = -\frac{E}{1-\nu^2}\left(\varepsilon_y + \nu\varepsilon_x\right) - \frac{E\alpha T(z)}{1-\nu}, \tag{3}$$

where σ_x is the longitudinal stress (MPa); σ_y is the transverse stress (MPa); E is Young's modulus (MPa); ν is Poisson's ratio; ε_x is the longitudinal strain ($\mu\varepsilon$); ε_y is the transverse strain ($\mu\varepsilon$); α is the CTE (/°C); and $T(z)$ is the temperature at the depth of z in the slab (°C).

Figure 6 presents a comparison between the computed stresses predicted by using the FE models and the measured stresses calculated by using equations (2) and (3). Here, S-measured and S-computed represent the measured stresses

Table 3: Material properties used in numerical analysis.

Structural components	Elastic modulus (E) (MPa)	Poisson's ratio (ν)	Density (ρ) (kg/m^3)
Concrete slab	34000	0.20	2400
CTB	2550	0.25	2200
CSB	1800	0.30	2200
Subgrade	150	0.35	1900
Dowel bar	200000	0.30	7850
Tension bar	200000	0.30	7850

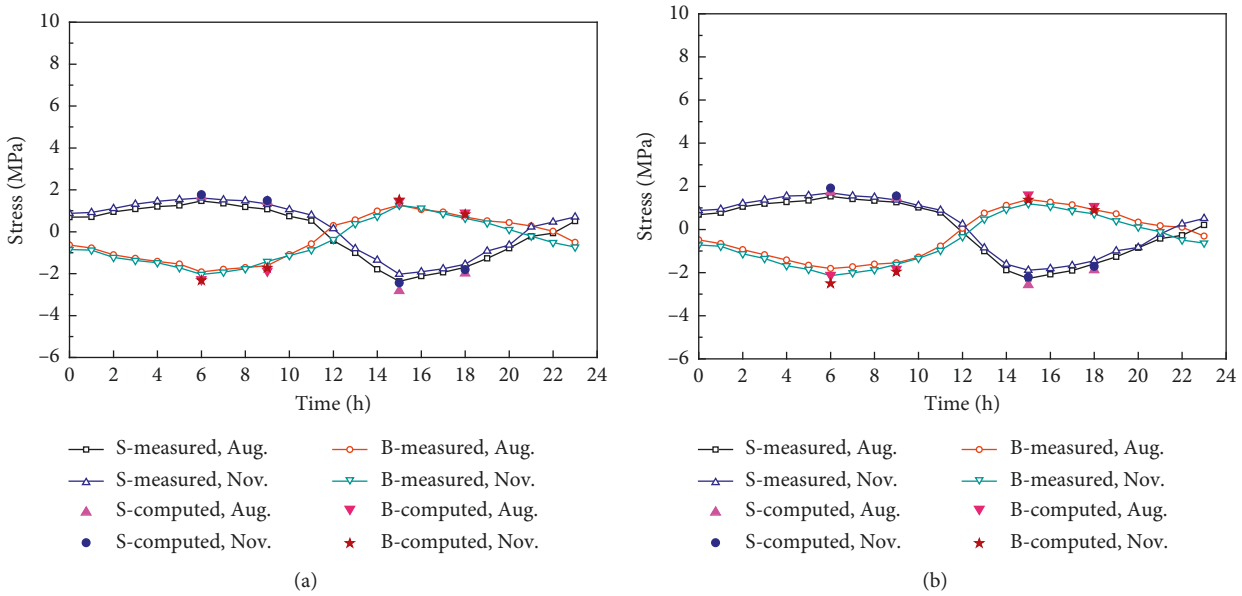

Figure 6: Measured and computed stresses in the concrete slab. (a) Stresses in the longitudinal direction. (b) Stresses in the transverse direction.

and computed stresses on the surface, respectively; B-measured and B-computed represent the measured stresses and computed stresses at the bottom, respectively. The results identify that the FE analysis results are in good agreement with the measured results in terms of the stress amplitude. The maximum difference of tensile stresses obtained by the two methods is 0.33 MPa in the longitudinal direction and 0.22 MPa in the transverse direction. Meanwhile, the maximum difference of compressive stresses is −0.41 MPa in the longitudinal direction and −0.37 MPa in the transverse direction. So, the FE method can effectively predict the mechanical properties of the concrete pavement.

4. Calculation Conditions considering the Temperature and Aircraft Loads

4.1. Aircraft Dynamic Load. The aircraft dynamic load is related to the sliding speed, the pavement roughness rating, and the lift of the wing. Lv et al. proposed an aircraft dynamic load coefficient model based on the International Roughness Index (IRI) [27]:

$$K' = 1 + 11.5c_0 IRI\sqrt{v} - \frac{1 + 11.5c_0 IRI\sqrt{v_0}}{v_0^2}v^2, \quad (4)$$

where K' is the aircraft dynamic load coefficient; $c_0 = 10^{-3}\,\mathrm{m}^{-0.5}\cdot\mathrm{s}^{0.5}$; v is the sliding speed; and v_0 is the instantaneous speed of aircraft taking-off.

The formula for solving the aircraft dynamic load is as follows:

$$F = K'G, \quad (5)$$

where F is the aircraft dynamic load and G is the aircraft static load (i.e., the maximum ramp weight).

The maximum allowable aircraft type is Boeing 737–800 in the design of the regional airport concrete pavement. Zhang et al. suggested that when $K' = 1$, the dynamic load is equal to the maximum ramp weight and the maximum ramp weight multiplied by $K' = 1.15$ is used as the maximum take-off weight of the Boeing 737–800 aircraft for the fatigue strength of the concrete pavement [28]. Commonly, the fatigue strength of the concrete material is much lower than the ultimate compressive strength [29]. Therefore, the maximum take-off weight (1.15 times the maximum ramp weight) is used as the dynamic load in the stress analysis of the concrete slabs based on the fatigue limit criterion, fully meeting the static strength requirements. The maximum dynamic load and related parameters of the B737-800 aircraft are listed in Table 4. Since the main landing gears

Table 4: Load and structure parameters of the B737-800 aircraft.

Related parameters	Value
Maximum aircraft dynamic load (kN)	790.04
Main landing gear number	2
Main landing gear configuration	Single axle dual wheel
Main landing gear distance (m)	5.72
Main landing gear wheelbase (m)	0.86
Tire pressure	1.47
Wheel seal area (m^2)	0.13
Wheel seal length (m)	0.43
Wheel seal width (m)	0.30

support 95% of the aircraft load, the aircraft load is assigned without considering the nose landing gear in the FE Models. Figure 7(a) shows a schematic illustration of the wheel configuration of the Boeing 737–800 aircraft, and Figure 7(b) shows the ground shape of the aircraft wheel, which is approximately composed of a rectangle and two semicircles.

4.2. Coupling of the Temperature and Aircraft Loads. Because the measured temperature is the temperature inside the concrete slab, the temperature difference between the surface and the bottom of the concrete slab is bigger. In numerical analysis, the positive and negative temperature gradients between the surface and the bottom of the concrete slab are set to $\pm 50^{\circ}C \cdot m^{-1}$ and $\pm 60^{\circ}C \cdot m^{-1}$, respectively.

When considering the combined effects of the temperature and aircraft loads, the most unfavorable load positions of the concrete slab are different. Related researches indicated that the longitudinal middle edge of the concrete slab is the most unfavorable area given positive temperature gradient and traffic load. However, the slab corner is the most unfavorable area given negative temperature gradient and traffic load [30, 31]. In this study, analysis is performed for two cases: (a) combined actions of positive temperature gradients and the single axle dual wheel load on the longitudinal middle edge of the concrete slab; (b) combined actions of negative temperature gradients and the single axle dual wheel load on concrete slab corner. Uniform area load is assigned in gravity direction to represent the single axle dual wheel load.

4.3. FE Model Calculation Cases. Because the width of the main landing gear of the Boeing 737–800 aircraft is 6.58 m, the main landing gear acts on separated slabs when the slab size is less than 3 m × 3 m, while the main landing gear acts on a single slab when the slab size is more than 6 m × 6 m. Figure 8 shows distributions of the single axle dual wheel load on concrete slabs with different sizes, only the case of slab longitudinal middle edge as shown in Figure 8. In addition, pavement design guidelines [21, 32] recommend that the thicknesses of concrete slab should not be less than 20 cm and the L/W ratios of slab should be 1~1.25. Vishwakarma and Ingle presented that most of the concrete pavements have a thickness below 35 cm [33]. They have also concluded that the critical stresses of the concrete slab

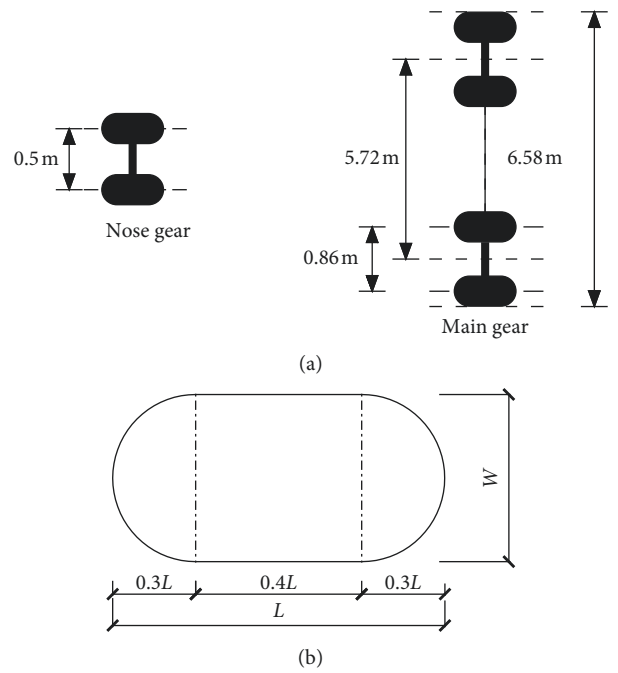

Figure 7: Wheel configuration of the Boeing 737–800 aircraft. (a) Landing gear. (b) Wheel ground shape.

for L/W ratio 1.25 or below are almost the same [20]. In this study, to optimize structural parameters of regional airport JCP, given the combined effect of large temperature gradient and aircraft loads, 144 numerical models were developed, as shown in Table 5.

5. Analysis of Results and Discussion

5.1. Determination of the Fatigue Limit. In the CACC guideline, equation (6) is used to analyze the fatigue life of concrete pavement. In addition, the NCHRP1 26 fatigue function (equation (7)) was recommended in the research report of the research and application of new technology for large military transportation airport pavement engineering construction conducted by the Tongji University. Equation (8) expresses the stress-strength ratio:

$$l_g(N) = 14.048 - 15.117e, \tag{6}$$

$$l_g(N) = \begin{cases} 4.284 - 1.7136e, & e > 1.25, \\ 2.8127e^{-1.2214}, & e \le 1.25, \end{cases} \tag{7}$$

$$e = \frac{\sigma}{f}, \tag{8}$$

where N is the fatigue life of the pavement slab; e is the stress-strength ratio; σ is the maximum tensile stress (MPa); and f is the flexural tensile strength (MPa).

According to the design requirements of the regional airport in Northeast China, the passenger handling capacity is 400,000 person times in a year. The maximum passenger volume of the Boeing 737–800 aircraft is 189 people. Therefore, the annual take-off times of the Boeing 737–800

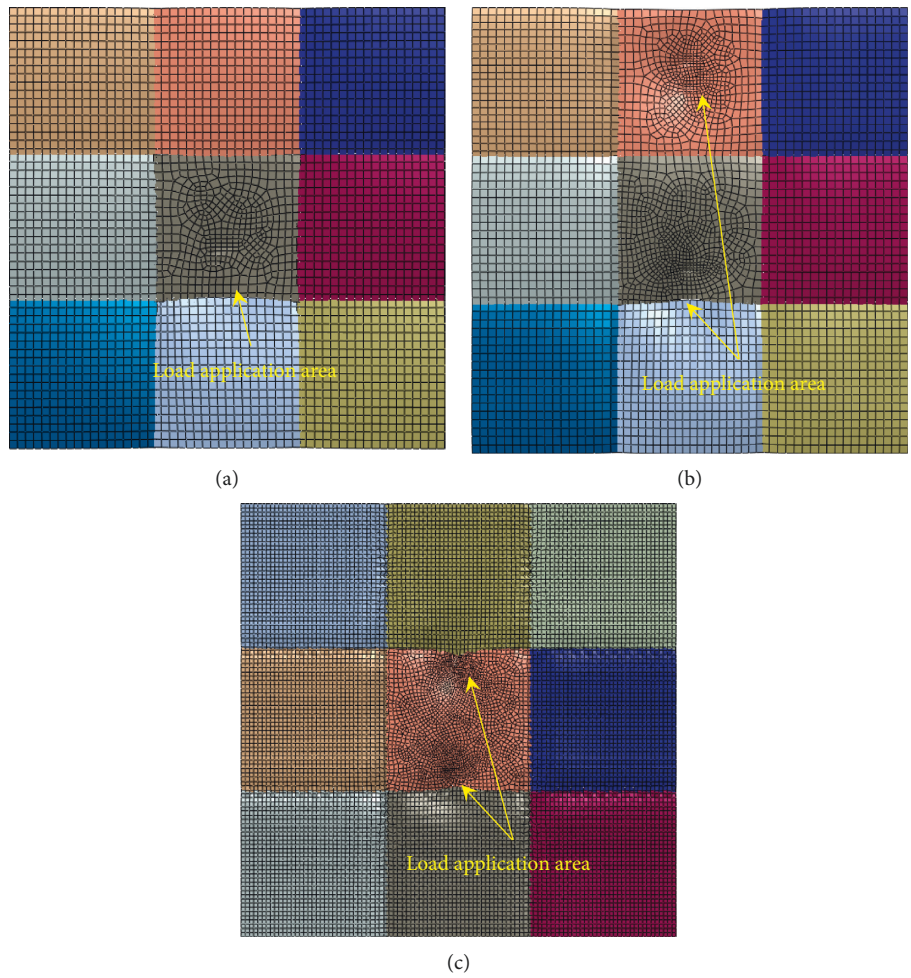

Figure 8: Distributions of the single axle dual wheel load on the concrete slabs with different sizes. (a) Load acting on separated slabs. (b) Load acting on adjacent slabs. (c) Load acting on a single slab.

Table 5: Statistics of numerical models.

Slab size	Thickness (cm)	L/W	Temperature gradient (°C·m^{-1})	Loading position
2 m × 2 m	20 25 30 35 40	1.00 1.05 1.10 1.15 1.20 1.25	50, −50, 60, −60	Longitudinal middle edge of slab or slab corner
3 m × 3 m				
4 m × 4 m				
5 m × 5 m				
6 m × 6 m				
7 m × 7 m				
8 m × 8 m				
9 m × 9 m				
Total				144 models

aircraft are determined as 2117 times. The designed service life of the airport pavement is 30 years, and thus $N = 2117 \times 30 = 63{,}510$ times. When compared with the results of stress-strength ratio as obtained by equations (6) and (7), the lower value is used that is $e = 0.61$. In this study, the flexural tensile strength of the concrete is 5.5 MPa. Thus, the fatigue limit of the concrete pavement is 3.3 MPa.

5.2. Optimization Analysis of Slab Size. Figure 9 shows the maximum tensile stresses computed by FE models of different slab sizes and thicknesses, given the unfavorable coupling of the temperature gradients (±60°C·m^{-1}) and the Boeing 737–800 aircraft load. The flexural tensile strength ($\sigma = 5.5$ MPa) and the fatigue limit ($f = 3.3$ MPa) of the concrete slabs are also denoted in Figure 9. The slab size has a significant influence on the maximum tensile stresses. The maximum tensile stresses are found to be increasing with the increase of the slab size. Compared with the maximum tensile stresses in 2 m × 2 m slab, those in 9 m × 9 m slab increase by 2.36 MPa under the combined effect of 60°C·m^{-1} and the slab edge load and 2.17 MPa under the combined effect of −60°C·m^{-1} and the slab corner load, respectively.

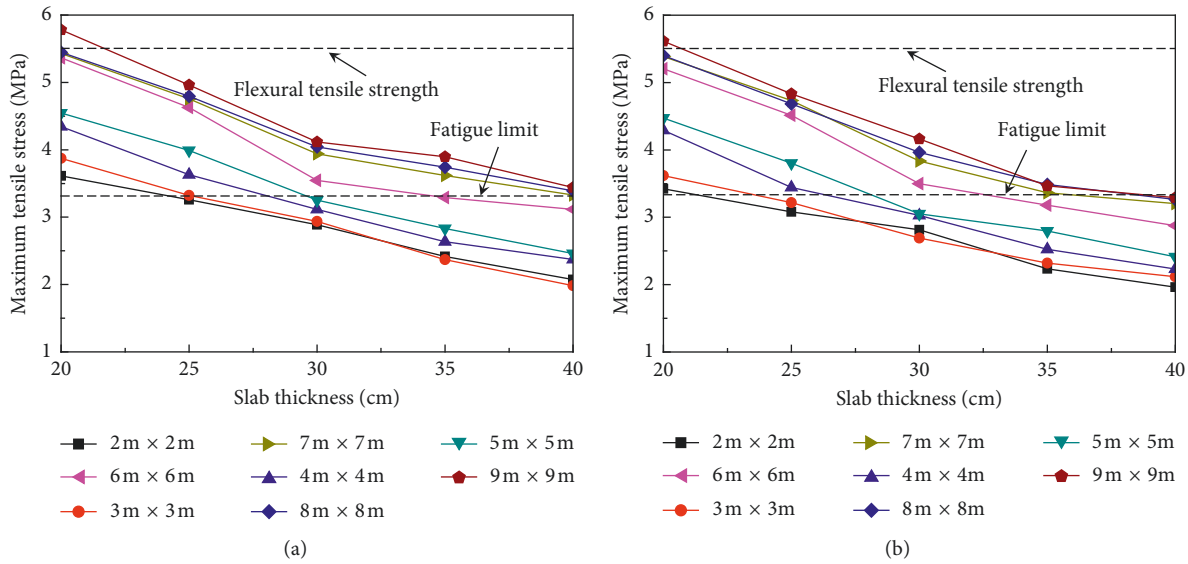

Figure 9: Maximum tensile stress given the combined effects of different temperature gradients and the aircraft load. (a) 60°C·m^{-1} and slab edge load. (b) −60°C·m^{-1} and slab corner load.

On the one hand, when the slab size is larger than 7 m × 7 m, the maximum tensile stresses are more than the fatigue limit under the combined effect of 60°C·m^{-1} and the slab edge load and more than or slight less than the fatigue limit under the combined effect of −60°C·m^{-1} and the slab corner load, respectively. On the other hand, the maximum tensile stresses in 2 m × 2 m slab and 3 m × 3 m slab are less. However, from the construction viewpoint, a decrease in the slab size inevitably increased the work of cutting joint and the amounts of materials such as dowel bars and tension bars. Consequently, the optimum slab sizes of the regional airport concrete pavement in Northeast China are recommended as 4 m × 4 m to 6 m × 6 m.

It also shows a sudden increase in the maximum tensile stress of 6 m × 6 m slab. This is because wheel is placed exactly at the edge for this width of slab. Thus, when the width of the concrete slab is close to the width of the main landing gear, the single axle dual wheel load acting on the key joints of both sides will easily cause greater tensile stress.

5.3. Optimization Analysis of Slab Thickness. As shown in Figure 9, the slab thicknesses also have a significant effect on the maximum tensile stress. The maximum tensile stress gradually decreases as the thickness of concrete slab increases. When the slab size is 9 m × 9 m, the maximum tensile stress in a 40 cm thick slab decreases by 2.34 MPa compared to that in a 20 cm thick slab under the combined effect of 60°C·m^{-1} and the slab edge load and by 2.22 MPa under the combined effect of −60°C·m^{-1} and the slab corner load, respectively. This is because the maximum tensile stress is related to the bending stiffness of the concrete slab. An increase in the bending stiffness decreases the maximum tensile stress [20, 33]. Moreover, the bending stiffness of the concrete slab is proportional to the third power of the slab thickness. Thus, an increase in the slab thickness increases the bending stiffness. The bending stiffness is expressed as follows [34]:

$$D = \frac{Eh^3}{12(1-\nu^2)}, \tag{9}$$

where D is the bending stiffness (N·m) and h is the slab thickness (m).

The concrete slabs with different sizes have different critical thicknesses under the same combined effect of the temperature gradient and aircraft loads. Figure 10 shows the critical thicknesses of concrete slabs, given the combined effects of different temperature gradients (±50°C·m^{-1} or ±60°C·m^{-1}) and the Boeing 737–800 aircraft load. Obviously, for the concrete slab with same size, the larger the temperature gradient, the larger the critical thickness required. The critical thicknesses of 4 m × 4 m slab and 6 m × 6 m slab are 28.2 cm and 34.7 cm, respectively, under the combined effect of 60°C·m^{-1} and the slab edge load. However, the critical thicknesses of 4 m × 4 m slab and 6 m × 6 m slab are 27.4 cm and 33.1 cm, respectively, under the combined effect of −60°C·m^{-1} and the slab corner load. Thus, with respect to the combined effects of ±60°C·m^{-1}and the Boeing 737–800 aircraft load, the critical thicknesses of 4 m × 4 m slab and 6 m × 6 m slab are determined as 28.2 cm and 34.7 cm, respectively.

5.4. Optimization Analysis of L/W Ratios. Figure 11 shows variations of maximum tensile stresses for different L/W ratios under the combined effects of 60°C·m^{-1} and the slab edge load or −60°C·m^{-1} and the slab corner load. The maximum tensile stress increases with the increase of the L/W ratio for the same width of concrete slab. This is because temperature stress gets added to aircraft load stress that enhances the total stress in the concrete slab. When the slab

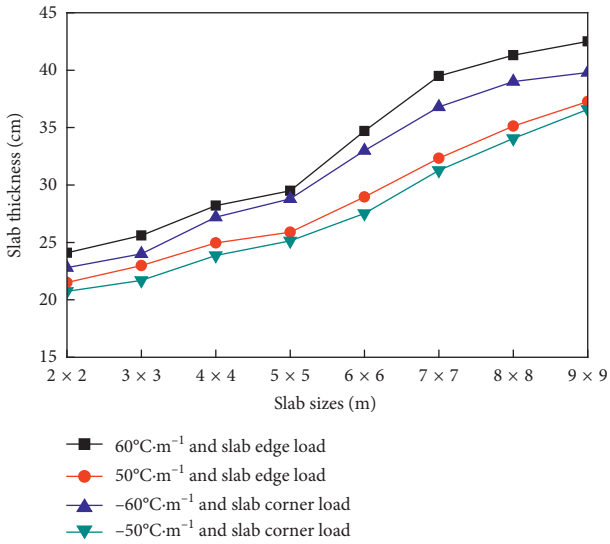

Figure 10: Critical thicknesses of concrete slabs given the combined effects of different temperature gradients and the aircraft load.

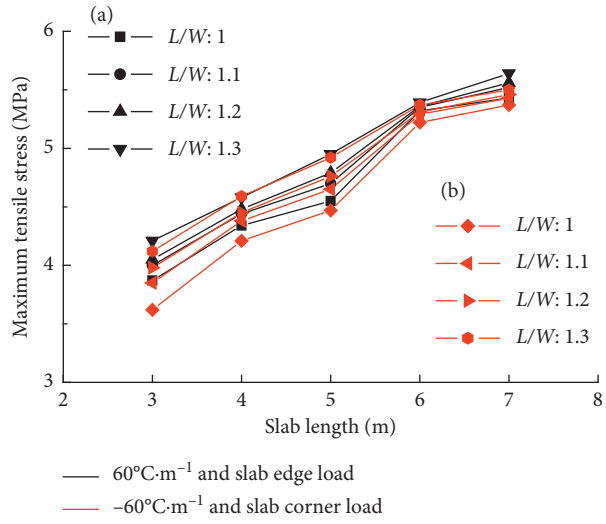

Figure 11: Variations of stresses for different L/W ratios due to the combined effects of different temperature gradients and the aircraft load.

length is less than 6 m, the maximum tensile stress in the slab for $L/W = 1.3$ increases by 0.50 MPa compared to that in the slab for $L/W = 1$. But, for the slab with a length of 6 m or 7 m, different L/W ratios have a slight effect on the maximum tensile stress. Consequently, when the slab length is less than 6 m, it is better to use square slab in airport JCP.

6. Conclusions

In order to optimize the structure parameters such as slab size, thickness, and L/W ratio of regional airport JCP, 3-D FE models were developed by using ABAQUS. The effects of different slab sizes, thicknesses, and L/W ratios on the maximum tensile stresses were investigated. In the numerical model, FE simulations of the environment gradient and Boeing 737–800 aircraft loads were modelled. Moreover, the environmental load was based on findings from the field temperature gradient. By analyzing the comparison results between the maximum tensile stress and the fatigue limit of the concrete slab, the following significant conclusions are made:

(1) The maximum tensile stresses alter largely as the structure parameters of JCP vary. The maximum tensile stress obtained is higher for larger slab size with thin thickness.

(2) With respect to the combined effects of the temperature and aircraft loads, unfavorable load-bearing positions, and construction factors, the optimum slab sizes of the regional airport concrete pavement are recommended as 4 m × 4 m to 6 m × 6 m.

(3) The critical thicknesses of 4 m × 4 m slab and 6 m × 6 m slab are determined as 28.2 cm and 34.7 cm, respectively, based on the comparison and analysis of calculation results of $60^{\circ}C \cdot m^{-1}$ and the slab edge load and $-60^{\circ}C \cdot m^{-1}$ and the slab corner load.

(4) When the slab length is less than 6 m, it is better to use square slab in regional airport JCP.

(5) Combined action of temperature gradient and aircraft loads induces higher stress. The larger the temperature gradient, the larger the critical thickness required. Hence, temperature load should not be neglected in the design of regional airport JCP where large temperature variations occur.

Data Availability

The figure data used to support the findings of this study have been deposited in the Figshare repository (https://figshare.com/articles/Academic_data/7379813). The table data used to support the findings of this study have been deposited in the Figshare repository (https://figshare.com/articles/Table_data/7379831).

Conflicts of Interest

The authors declare that there are no conflicts of interest.

Authors' Contributions

Bangshu Xu and Wanzhi Zhang conceived and designed the experiments. Wanzhi Zhang and Guangyao Yue analyzed the data and made numerical simulation. Wanzhi Zhang and Jie Mei wrote the paper. Laihua Yang contributed experimental sites.

Acknowledgments

This research was supported by the National Nature Science Foundation of China (Grant no. 50909056).

References

[1] X. Ma, F. J. Ni, and X. Y. Gu, "Structure design method of composition airfield pavement," *Journal of Traffic and Transportation Engineering*, vol. 10, no. 2, pp. 36–40, 2010.

[2] M. Q. Jin, "Research on typical diseases analysis and treatment technology of airport cement concrete pavement," Master's thesis, Chang'an University, Xi'an, China, 2015.

[3] S.-M. Kim and J.-H. Nam, "Measurements and experimental analysis of temperature variations in Portland cement concrete pavement systems," *Road Materials and Pavement Design*, vol. 11, no. 3, pp. 745–771, 2010.

[4] Y. Qin and J. E. Hiller, "Simulating moisture distribution within concrete pavement slabs: model development and sensitivity study," *Materials and Structures*, vol. 47, no. 1-2, pp. 351–365, 2014.

[5] Y. Qin and J. E. Hiller, "Modeling the temperature and stress distributions in rigid pavements: impact of solar radiation absorption and heat history development," *KSCE Journal of Civil Engineering*, vol. 15, no. 8, pp. 1361–1371, 2011.

[6] S.-H. Kim, J.-Y. Park, and J.-H. Jeong, "Effect of temperature-induced load on airport concrete pavement behavior," *KSCE Journal of Civil Engineering*, vol. 18, no. 1, pp. 182–187, 2014.

[7] D. H. Chen and M. Won, "Field investigations of cracking on concrete pavements," *Journal of Performance of Constructed Facilities*, vol. 21, no. 6, pp. 450–458, 2007.

[8] O. M. Jensen and P. F. Hansen, "Influence of temperature on autogenous deformation and relative humidity change in hardening cement paste," *Cement and Concrete Research*, vol. 29, no. 4, pp. 567–575, 1999.

[9] J. H. Jeong and D. G. Zollinger, "Environmental effects on the behavior of jointed plain concrete pavements," *Journal of Transportation Engineering*, vol. 131, no. 2, pp. 140–148, 2005.

[10] H. J. Oh, Y. K. Cho, Y. Seo, and S.-M. Kim, "Experimental analysis of curling behavior of continuously reinforced concrete pavement," *Construction and Building Materials*, vol. 128, pp. 57–66, 2016.

[11] H. M. Westergaard, "Analysis of stresses in concrete pavements due to variations of temperature," *Highway Research Board Proceedings*, vol. 6, pp. 201–215, 1927.

[12] P. Mackiewicz, "Thermal stress analysis of jointed plane in concrete pavements," *Applied Thermal Engineering*, vol. 73, no. 1, pp. 1169–1176, 2014.

[13] M. Belshe, M. S. Mamlouk, K. E. Kaloush, and M. Rodezno, "Semperature gradient and curling stresses in concrete pavement with and without open-graded friction course," *Journal of Transportation Engineering*, vol. 137, no. 10, pp. 723–729, 2011.

[14] B. Tian, L. Quan, and K. M. Niu, "Structural experiment and theoretical analysis of thermal curling in JPCP with different base types," *China Journal of Highway and Transport*, vol. 27, no. 6, pp. 17–26, 2014.

[15] B. H. Nam, J. H. Yeon, and Z. Behring, "Effect of daily temperature variations on the continuous deflection profiles of airfield jointed concrete pavements," *Construction and Building Materials*, vol. 73, pp. 261–270, 2014.

[16] Y. H. Huang, *Pavement Analysis and Design*, Pearson Education Inc., Hoboken, NJ, USA, 2nd edition, 2004.

[17] Y. Wei, S. M. Liang, K. He, and J. L. Feng, "Slab-size optimization of rural road concrete pavement considering the combined effect of temperature gradient and traffic load," *Engineering Mechanics*, vol. 32, no. 7, pp. 111–142, 2015.

[18] R. Chattaraj and B. B. Pandey, "Short panelled concrete pavement in built-up area," *Indian Highways*, vol. 42, no. 1, pp. 5–12, 2014.

[19] M. Al-Nasra and L. R. L. Wang, "Parametric study of slab-on-grade problems due to initial warping and point loads," *ACI Structural Journal*, vol. 91, no. 2, pp. 198–210, 1994.

[20] R. J. Vishwakarma and R. K. Ingle, "Effect of panel size and radius of relative stiffness on critical stresses in concrete pavement," *Arabian Journal for Science and Engineering*, vol. 43, no. 10, pp. 5677–5687, 2018.

[21] China Airport Construction Group Corporation (CACC), *Specifications for Airport Cement Concrete Pavement Design, MH/T5004-2010*, China Communication Press, Beijing, China, 2010.

[22] Z. F. Zhou and J. M. Ling, "Finite element model of airport rigid pavement structure based on ABAQUS," *Journal of Traffic and Transportation Engineering*, vol. 19, no. 3, pp. 39–44, 2009.

[23] H. J. Oh, S.-M. Kim, W. Chung, Y. H. Lee, and Y. K. Cho, "Effect of joint type on rigid airfield pavement behavior," *KSCE Journal of Civil Engineering*, vol. 18, no. 8, pp. 1389–1396, 2014.

[24] Dassault Systèmes Simulia Corp, *ABAQUS User's Manual, Version 6.13-1*, Dassault Systèmes Simulia Corp., Providence, RI, USA, 2013.

[25] B. Choubane and M. Tia, "Analysis and verification of thermal-gradient effects on concrete pavement," *Journal of Transportation Engineering*, vol. 121, no. 1, pp. 75–81, 1995.

[26] S. P. Timoshenko and S. Woinowsky-Krieger, *Theory of Plates and Shells*, McGraw-Hill Book Co. Inc., New York, NY, USA, 1959.

[27] Y. Z. Lv, Q. Dong, C. F. Hu, M. S. Li, and J. G. Zhang, "Study on the relationship between aircraft dynamic load and international roughness index," *Journal of China and Foreign Highway*, vol. 33, no. 3, pp. 74–77, 2013.

[28] X. M. Zhang, Q. Dong, Y. Z. Lv, H. X. Xue, and Z. C. Sun, "Mechanical responses of edge of rigid airport pavement under aircraft loadings," *Journal of Nanjing University of Aeronautics and Astronautics*, vol. 45, no. 5, pp. 693–699, 2013.

[29] K. Dyduch, M. Szerszeń, and J.-F. Destrebecq, "Experimental investigation of the fatigue strength of plain concrete under high compressive loading," *Materials and Structures*, vol. 27, no. 9, pp. 505–509, 1994.

[30] K. Kim and S. Chun, "Evaluation of internally cured concrete pavement using environmental responses and critical stress analysis," *International Journal of Concrete Structures and Materials*, vol. 9, no. 4, pp. 463–473, 2015.

[31] B. Qu, X.-Z. Weng, J. Zhang et al., "Analysis on the deflection and load transfer capacity of a prefabricated airport pre-stressed concrete pavement," *Construction and Building Materials*, vol. 157, pp. 449–458, 2017.

[32] American Association of State Highway, and Transportation Officials, *AASHTO Guide for Design of Pavement Structures*, American Association of State Highway, Washington, DC, USA, 1993.

[33] R. J. Vishwakarma and R. K. Ingle, "Simplified approach for the evaluation of critical stresses in concrete pavement," *Structural Engineering and Mechanics*, vol. 61, no. 3, pp. 389–396, 2017.

[34] Z. K. Yao, *Highway Design Manual—Pavement*, China Communications Press, Beijing, China, 2006.